Nanoscale Advances

ROYAL SOCIETY OF CHEMISTRY

PAPER

View Article Online
View Journal | View Issue

Cite this: *Nanoscale Adv.*, 2025, **7**, 7740

Bimetallic $MgFe_2O_4$@BiBTC hybrids for efficient photocatalytic degradation of rhodamine B

Van Cuong Nguyen, *[a] Ai Le Hoang Pham, [a] Trinh Duy Nguyen, [bc] Huynh Dao Thanh Dreaml,[a] Thi Huyen Thoa Pham[d] and Nguyen Thi Mai Tho *[a]

This study involved the incorporation of magnesium ferrite ($MgFe_2O_4$) nanoparticles into a bismuth-based metal–organic framework (BiBTC) to develop a novel magnetic photocatalyst, $MgFe_2O_4$@BiBTC, *via* a solvothermal approach. The $MgFe_2O_4$@BiBTC structural, optical, magnetic, and surface characteristics were thoroughly examined using XRD, FT-IR, SEM-EDS, TEM, XPS, UV-vis DRS, and VSM techniques. The findings indicated that $MgFe_2O_4$ in conjunction with BiBTC at a mass ratio of 20% (MFB20) exhibited the highest efficiency in Rhodamine B (RhB) decomposition, achieving 97.98%, under the parameters of catalyst mass 10 mg, RhB concentration 20 mg L^{-1}, volume 50 mL, adsorption duration 60 min, and LED illumination time 120 min. The degradation rate of RhB of MFB20 (k = 0.03458 min^{-1}) was about 1.5-fold higher than that of pristine BiBTC (k = 0.02334 min^{-1}). The enhanced activity is attributed to a type-II heterojunction between $MgFe_2O_4$ and BiBTC that drives electron transfer and photogenerated hole formation at the interface of the two phases, therefore enhancing charge separation and minimizing recombination, which improves the degradation efficiency of RhB. Radical scavenging tests found superoxide radicals ($^{\bullet}O_2^-$) as the most reactive species. Although MFB20 shows a reduced saturation magnetization relative to $MgFe_2O_4$, the coercivity remains essentially unchanged, indicating that the ferrite phase maintains its magnetic integrity within the composite.

Received 12th August 2025
Accepted 13th October 2025

DOI: 10.1039/d5na00774g

rsc.li/nanoscale-advances

Introduction

Rhodamine B (RhB) is an organic dye extensively used in chemistry and biology, particularly within the textile, food, and biological dye fields. Despite its many beneficial uses, substantial releases of RhB into the environment may inflict significant damage on natural systems and pose risks to aquatic organisms and human health.[1–3] Direct contact with RhB induces allergic reactions or irritation to the skin and eyes, while ingestion *via* the digestive system results in vomiting, liver and kidney damage, and potential carcinogenic effects.[4] Consequently, while increasing awareness of environmental conservation, researchers are also exploring methods to remediate these contaminants. The removal of RhB contaminant has been investigated through various methodologies, including ion exchange, biodegradation, ozonation, electrochemical oxidation, adsorption, and semiconductor-based photocatalytic degradation.[5] Among them, advanced oxidation processes (AOPs) using semiconductor photocatalysts are a notable method because of their capacity to harness solar energy and their potent oxidation capabilities.[6–9] Nonetheless, photocatalysts often present challenges in recycling and may produce secondary pollutants. To address this issue, researchers have proposed the development of photocatalysts that may be readily recovered by applying an external magnetic field.[9–11]

Magnesium ferrite ($MgFe_2O_4$), characterized as a spinel ferrite (AFe_2O_4), has outstanding magnetic, electrical, and optical capabilities due to the distribution of Mg^{2+} and Fe^{3+} cations between the tetrahedral (A) and octahedral (B) sites within its spinel structure.[12] Furthermore, $MgFe_2O_4$ has remarkable stability in both acidic and basic environments, facilitating its efficient retrieval as a solid from a liquid mixture by applying a magnetic field. Utilizing $MgFe_2O_4$ has garnered significant interest from academics because of its distinctive magnetic and photocatalytic characteristics.[13,14] Zhang and colleagues synthesized $MgFe_2O_4/TiO_2$ composites with 2 wt% and 3 wt% MFO loading *via* a mixing-annealing technique. The resulting heterostructures exhibited markedly improved photocatalytic performance under visible light irradiation for the degradation of rhodamine B in comparison with the individual $MgFe_2O_4$ and TiO_2 components.[15] The enhanced performance of the photocatalysts was primarily attributed to the synergistic interaction between the two semiconductors, whose band

[a]*Faculty of Chemical Engineering, Industrial University of Ho Chi Minh City, No. 12 Nguyen Van Bao, Hanh Thong Ward, Ho Chi Minh City, Vietnam. E-mail: nvc@iuh.edu.vn; nguyenthimaitho@iuh.edu.vn*

[b]*Center for High Technology Development, Nguyen Tat Thanh University, Ho Chi Minh City Hi-Tech Park, Ho Chi Minh City, Vietnam*

[c]*Institute of Applied Technology and Sustainable Development, Nguyen Tat Thanh University, Ho Chi Minh City, Vietnam*

[d]*Department of Natural Sciences & Technology, Tay Nguyen University, DakLak Province 630000, Vietnam*

potentials were suitably aligned. Moreover, $MgFe_2O_4/TiO_2$ enhanced the deficiencies of ferrite materials, such as inadequate adsorption effectiveness for pollutants resulting from limited surface area and pore volume. Additionally, $MgFe_2O_4/TiO_2$ also enhanced the drawbacks of ferrite materials, such as their poor adsorption effectiveness for contaminants, because of their small surface area and pore volume.[16,17]

The BiBTC metal–organic framework, consisting of bismuth centers coordinated with the H_3BTC linker, has been structurally classified as CAU-17 and UU-200 types.[18,19] Photocatalytic studies reveal that BiBTC possesses a relatively wide bandgap (3.2–3.6 eV) and suffers from inefficient ligand-to-metal charge transfer, particularly from the excited organic linkers to the Bi–O clusters.[20,21] As a result, strategies to improve its photocatalytic activity under visible light are necessary to broaden its applicability in photochemical processes. Various modification approaches have been explored, including ligand functionalization and the incorporation of noble metals or metal oxides into the MOF structure. Notably, a composite of the UU-200 framework with graphitic carbon nitride ($g\text{-}C_3N_4$) exhibited enhanced rhodamine B degradation under simulated solar irradiation.[22] This improvement is attributed to the synergistic interaction between the two semiconductors, facilitating more efficient charge separation and transfer while suppressing the recombination of photogenerated electron–hole pairs.

This study, $MgFe_2O_4$@BiBTC composites were synthesized *via* a solvothermal approach by integrating $MgFe_2O_4$ ferrite nanoparticles with the BiBTC framework, comprising CAU-17 and UU-200 structural motifs. $MgFe_2O_4$@BiBTC integrates efficient charge separation with magnetic recyclability, delivering faster, cleaner, and more practical RhB photodegradation than pristine BiBTC. The physicochemical properties of the resulting composites were systematically characterized using a range of analytical techniques. The photocatalytic performance of $MgFe_2O_4$@BiBTC was then evaluated through the degradation of rhodamine B under visible light irradiation, focusing on assessing the influence of key operational parameters. The photocatalytic degradation mechanism was also proposed based on the interaction between BiBTC and $MgFe_2O_4$ components. This work represents the first investigation into the synergistic enhancement of RhB photodegradation by coupling $MgFe_2O_4$ ferrite with the BiBTC framework to form $MgFe_2O_4$@BiBTC composites.

Material and method

Materials

$Bi(NO_3)_3\cdot 5H_2O$ (≥98.0%), H_3BTC ($C_9H_6O_6$, 95.0%), $MgCl_2\cdot 6H_2O$ (≥98.0%), $FeCl_3\cdot 6H_2O$ (97%), $C_{19}H_{42}BrN$ (≥96.0%), RhB ($C_{28}H_{31}ClN_2O_3$, ≥95.0%), and *p*-benzoquinone (BQ, $C_6H_4O_2$, ≥99.0%) were obtained from Sigma-Aldrich. Dichloromethane (DCM, CH_2Cl_2, ≥99.7%), *N*,*N*-dimethylformamide (DMF, C_3H_7NO, ≥99.8%), ethanol (EtOH, C_2H_6O, ≥99.7%), isopropanol (IPA, C_3H_8O, ≥99.7%), sodium oxalate ($Na_2C_2O_4$, ≥99.8%), potassium dichromate ($K_2Cr_2O_7$, ≥99.8%), and methanol (MeOH, CH_4O, ≥99.7%) were obtained from Xilong Scientific Co. Ltd. Deionized water from the Thermo Scientific Micro Pure system was used throughout the experiment. All chemicals used in this study were obtained as received and without additional purification.

Synthesis of $MgFe_2O_4$

$MgFe_2O_4$ nanoparticles were synthesized *via* a co-precipitation method. Initially, 1.02 g of $MgCl_2\cdot 6H_2O$ and 2.745 g of $FeCl_3\cdot 6H_2O$ were dissolved in 50 mL of deionized water under continuous stirring. Then, 1.833 g of cetyltrimethylammonium bromide (CTAB) was added as a surfactant, followed by ultrasonication for 15 min to ensure homogeneity. The resulting solution was transferred into a 250 mL round-bottom flask, and 25 mL of 10 M NaOH was added dropwise under constant stirring. The mixture was maintained at 70 °C and stirred for 24 h to facilitate the formation of the ferrite phase. The resulting precipitate was filtered, repeatedly washed with deionized water until a neutral pH was achieved, and dried at 100 °C. The dried powder was ground and calcined at 700 °C for 4 h to obtain crystalline $MgFe_2O_4$ nanoparticles, referred to as sample MF.

Synthesis of hybrid $MgFe_2O_4$@BiBTC composite

The $MgFe_2O_4$@BiBTC composites were synthesized *via* a solvothermal route. In a typical procedure, 0.15 g of $Bi(NO_3)_3$ and 0.75 g of H_3BTC were dissolved in 60 mL of a 1 : 1 methanol (MeOH) and *N*,*N*-dimethylformamide (DMF) mixture. To this solution, 0.015 g of $MgFe_2O_4$ nanoparticles was uniformly dispersed using ultrasonic agitation for 15 minutes. The resulting suspension was transferred into a Teflon-lined autoclave and heated at 120 °C for 24 hours. After the reaction, the solid product was washed several times with a 1 : 1 DMF/MeOH solvent mixture and dried at 80 °C for 24 h, yielding the $MgFe_2O_4$@BiBTC composite, designated as sample MFB10. For comparison, composites with higher ferrite content were prepared using the same procedure, adjusting the $MgFe_2O_4$ mass to 0.03 g and 0.045 g to obtain samples MFB20 and MFB30, respectively. The pure BiBTC framework was synthesized separately according to the procedure described in the supplementary section, following previously reported methods.[23]

Material characterization

The structural and physicochemical properties of the samples and their constituents were characterized using various analytical techniques. X-ray diffraction (XRD) patterns were recorded with Cu Kα radiation over a 2θ range of 5° to 80°, with a step size of 0.02°, to investigate the crystalline phases. Fourier-transform infrared (FT-IR) spectra were obtained using a Bruker Tensor 27 spectrometer to identify functional groups and coordination environments in the 500–4000 cm^{-1} range. Room-temperature magnetic behavior was evaluated using a vibrating sample magnetometer (VSM, Model JDM-13). Thermal stability was assessed under a nitrogen atmosphere with a heating rate of 10 °C min^{-1} using a thermogravimetric analyzer (TGA, Q50, TA Instruments, USA). X-ray photoelectron spectroscopy (XPS) measurements were conducted on an AXIS SUPRA system

(Kratos Analytical Ltd) to analyze surface composition and oxidation states. Morphological features and elemental distribution were examined *via* scanning electron microscopy (SEM) coupled with energy-dispersive X-ray spectroscopy (EDS), using a JEOL JSM-IT800 microscope. Ultraviolet-visible diffuse reflectance spectroscopy (UV-vis DRS) was carried out using a Cary 4000 UV-vis spectrophotometer to determine the optical absorption properties.

Photocatalytic degradation experiment

The photocatalytic performance of the synthesized materials was systematically evaluated through the degradation of rhodamine B (RhB) under simulated solar irradiation. A 40 W LED light source (Cree Inc., Durham, NC, USA) with dimensions of 3.45 × 3.45 × 2.36 mm and an irradiance of 141 W m^{-2} served as the illumination source. All photocatalytic reactions were carried out in a 250 mL double-jacketed glass reactor maintained at ambient temperature *via* a circulating water system. The entire setup was enclosed within a lightproof box lined with aluminum foil to eliminate external light interference. For each photocatalytic run, 10 mg of the photocatalyst and 50 mL of an aqueous RhB solution (20 mg L^{-1}) were added to the reactor and stirred in the dark for 60 min to ensure adsorption–desorption equilibrium. Upon exposure to simulated visible light, the suspension was continuously stirred, and aliquots of 3 mL were withdrawn at 15 min intervals. The catalyst was magnetically separated, and the supernatant was analyzed using a UV-vis spectrophotometer by monitoring the absorbance at 554 nm to determine the residual RhB concentration. To optimize the degradation conditions, various operational parameters were investigated, including the $MgFe_2O_4$/BiBTC mass ratio (MF, MFB10, MFB20, MFB30, and BiBTC), catalyst dosage, initial RhB concentration, and pH of the reaction medium. The degradation kinetics were fitted to a pseudo-first-order model, expressed as $\ln(C_0/C_t) = kt$, where C_0 and C_t (mg L^{-1}) represent the initial and instantaneous RhB concentrations. The apparent rate constant (k, min^{-1}) and correlation coefficient (R^2) were derived from the linear regression of the kinetic data.

To elucidate the primary reactive species involved in the photocatalytic degradation process, specific scavengers were employed: ethanol (EtOH) for hydroxyl radicals ($^{\bullet}OH$), benzoquinone (BQ) for superoxide radicals ($^{\bullet}O_2^-$), potassium dichromate ($K_2Cr_2O_7$) for electrons (e^-), and sodium oxalate ($Na_2C_2O_4$) for photogenerated holes (h^+). A 3 mL aliquot of each scavenger solution (100 μM) was introduced into the RhB photodegradation system at the initiation of light irradiation. Additionally, the reusability of the photocatalyst was assessed through recycling experiments. After each photodegradation cycle, the MFB composite was separated *via* centrifugation, thoroughly washed with ethanol and deionized water to remove residual dye and reaction intermediates, and subsequently dried at 80 °C for 12 h before reuse in the next photocatalytic run. The experiments were conducted separately and repeated three times ($n = 3$), with the average result used for calculation. The error in the graphs was ascertained using the standard deviation (SD).

Results and discussion

Material characterization

Fig. 1a presents the XRD patterns of the pristine $MgFe_2O_4$ (MF), BiBTC, and their composites with varying MF contents (MFB10, MFB20, and MFB30). The diffraction peaks of pure MF match well with the standard spinel structure of $MgFe_2O_4$, exhibiting characteristic reflections at $2\theta \approx 18.3°$, 30.3°, 35.6°, 43.3°, 53.6°, 57.3°, and 62.9°, corresponding to the (111), (220), (311), (400), (422), (511), and (440) planes, respectively (JCPDS no. 89-4924). These peaks confirm the successful formation of crystalline spinel ferrite.[24] In contrast, the BiBTC framework shows distinct diffraction peaks indicative of its crystalline nature, with sharp reflections between 5° and 30°, typical of Bi-MOFs, which align with previously reported data for a mixed-phase system comprising the CAU-17 (CCDC no. 1426169) and UU-200 (CCDC no. 2103784) metal–organic frameworks.[18,19] These reflections are retained in the MFB composites, suggesting the structural integrity of BiBTC is preserved after MF incorporation. For the MFB composites (MFB10, MFB20, and MFB30), the diffraction patterns exhibit characteristic peaks corresponding to both $MgFe_2O_4$ and BiBTC, indicating the co-existence of the two phases without the formation of new crystalline impurities. However, the intensity of peaks associated with BiBTC diminished markedly with increasing MF content in the MBF samples, indicating that MF was effectively dispersed on the BiBTC surface, covering a portion of crystallinity or structural alterations in the BiBTC matrix upon the incorporation of ferrite nanoparticles. Conversely, the MF-associated peaks become more prominent at higher loading, particularly in the MFB30 sample, reflecting the increasing contribution of the ferrite phase in the hybrid composite.

Fig. 1b presents the FT-IR spectra of pure MF, BiBTC, and their composites (MFB10, MFB20, and MFB30). The spectrum of MF shows two prominent absorption bands at 575 cm^{-1} and 435 cm^{-1}, attributed to the stretching vibrations of M–tetra–O and M–octa–O bonds in the spinel ferrite structure of $MgFe_2O_4$, respectively, confirming its typical crystalline ferrite phase.[24,25] The BiBTC spectrum exhibits characteristic peaks in the 1300–1750 cm^{-1} region, corresponding to the asymmetric and symmetric stretching vibrations of the carboxylate groups coordinated with Bi^{3+} centers. A distinct band at approximately 519 cm^{-1} is assigned to the O–Bi–O bending vibration, a fingerprint feature of the Bi-based coordination environment in the MOF framework.[21] In the spectra of the MFB composites, the coexistence of features from both $MgFe_2O_4$ and BiBTC is evident. The presence of ferrite is confirmed by the retention of the metal–oxygen stretching bands near 575 and 435 cm^{-1}, while the MOF structure is indicated by the persistence of carboxylate and O–Bi–O bands. Notably, a reduction in peak intensity is observed for the BiBTC-related vibrations in the MFB samples compared to pure BiBTC. The reduced intensity of BiBTC-related peaks in the MFB samples indicates successful ferrite incorporation with partial attenuation of MOF features.

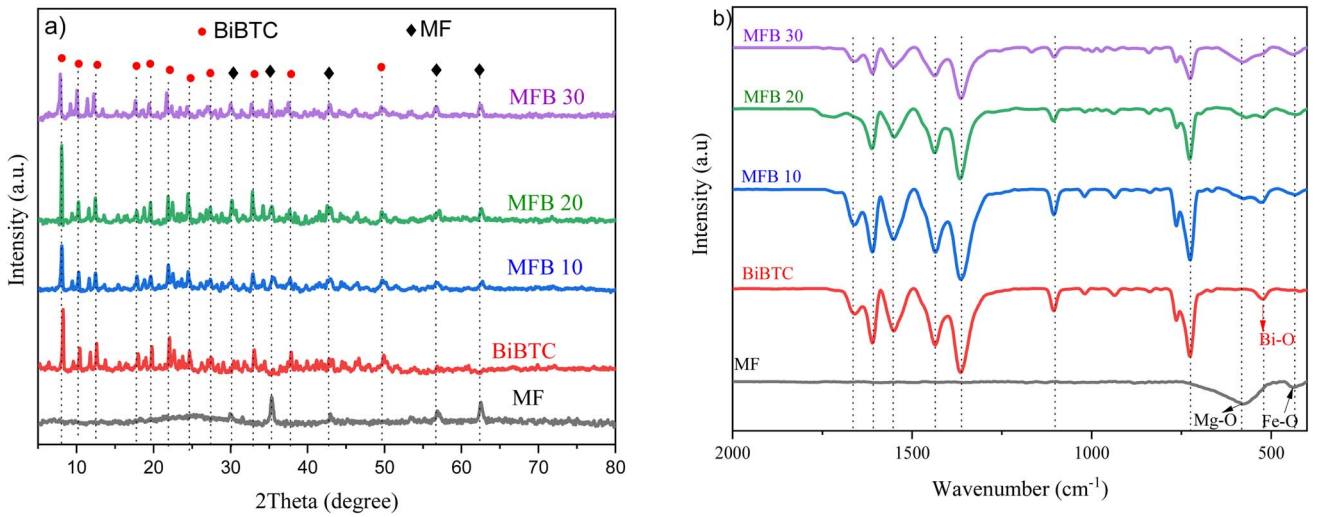

Fig. 1 (a) XRD patterns and (b) FT-IR of the as-synthesized samples.

These results confirm the structural integration of both components in the composite.

Fig. 2 shows the magnetic hysteresis loops of MF and MFB composites. MF exhibits strong ferromagnetism with a saturation magnetization (M_s) of ~40 emu g^{-1}, coercivity (H_c) of ~110 Oe, and remanence (M_r) of 12.5 emu g^{-1}. Upon BiBTC incorporation, M_s values decrease to ~22.8, 17.5, and 13.2 emu g^{-1} for MFB10, MFB20, and MFB30, respectively, due to magnetic dilution. Despite the reduction in saturation magnetization, key magnetic properties like coercivity remained stable, indicating that magnesium ferrite retains its stability within the composite MFB. The composites retain soft magnetic behavior with sufficient response for magnetic separation, as demonstrated in the inset. These results confirm successful integration of $MgFe_2O_4$ while maintaining magnetic recoverability for practical reuse.

The MF sample demonstrates excellent thermal stability, with negligible weight loss (<5%) observed across the entire temperature range (25–700 °C), indicating the robustness of the spinel ferrite structure. In contrast, the BiBTC sample shows a two-step weight loss behavior. The first stage (up to ~350 °C) corresponds to removing adsorbed moisture and guest molecules, accounting for ~15.56% weight loss. The second and significant weight loss (~43.50%) occurs between 350 and 550 °C, attributed to the decomposition of the organic linker and collapse of the MOF framework, leaving behind a metal oxide residue. The MFB composite exhibits a similar decomposition profile to BiBTC, with an initial weight loss of ~13.33% due to desorption of water and volatile species, followed by a significant loss of ~36.37% in the 350–550 °C range, reflecting partial decomposition of the BiBTC matrix. The total weight loss of MFB is notably lower than that of pure BiBTC, owing to the presence of thermally stable $MgFe_2O_4$, which acts as an inorganic scaffold enhancing the overall thermal resistance of the composite (Fig. 3a). These results confirm the successful hybridization of BiBTC with $MgFe_2O_4$ and highlight the improved thermal stability of the MFB composite compared to pure BiBTC, which is beneficial for applications requiring elevated operational temperatures.[19,26]

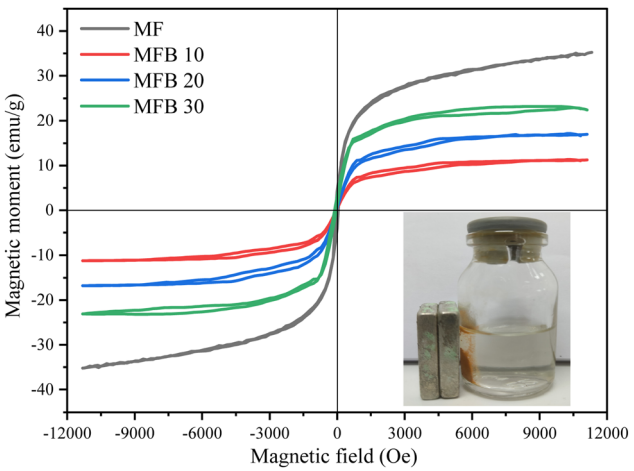

Fig. 2 Magnetic hysteresis curve of MF and MFB samples at room temperature. The inset shows the magnetic separation property of MFB.

Fig. 3b illustrates the determination of the point of zero charge (pH_{pzc}) for $MgFe_2O_4$, BiBTC, and the MFB composite. The pH_{pzc} values were determined to be approximately 5.2 for MF, 4.4 for BiBTC, and 5.7 for the MFB composite. These values suggest that at pH values below the pH_{pzc}, the material surfaces are positively charged, while at pH values above pH_{pzc}, they become negatively charged. The slight shift of the pH_{pzc} in MFB toward a higher value than its individual components indicates the influence of ferrite integration on the surface charge distribution. The increase in pH_{pzc} can be attributed to the fundamental nature of $MgFe_2O_4$, which partially neutralizes the acidic functional groups in BiBTC.

X-ray photoelectron spectroscopy (XPS) was employed to investigate the surface elemental composition and chemical states of the MFB composite. The survey spectrum confirms the presence of Mg, Fe, O, Bi, and C elements, verifying the

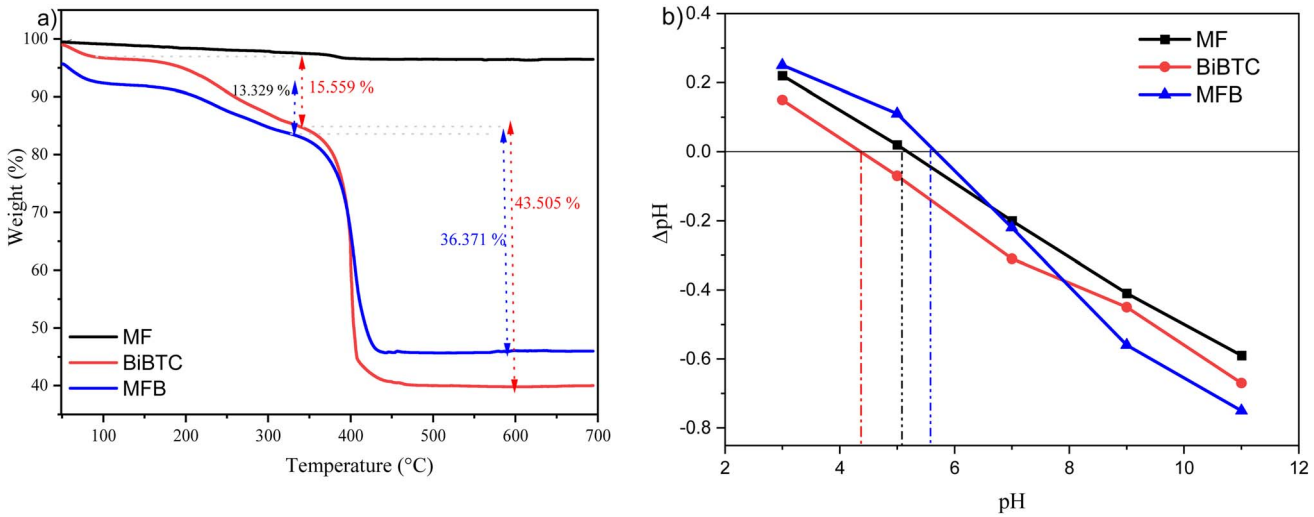

Fig. 3 (a) TGA and (b) zeta potential analyses of the synthesized samples.

successful integration of $MgFe_2O_4$ and BiBTC components (Fig. 4). The high-resolution C 1s spectrum (Fig. 4b) of the CAU-17 component reveals three distinct peaks at 282.6 eV, 286.2 eV, and 301.8 eV, which can be assigned to C=C/C–C, C–O, and C=O species, respectively, consistent with the bonding environment of the BTC linker.[27] The O 1s spectra (Fig. 4c) reveal four primary peaks at 529.14 eV, 529.79 eV, 530.38 eV, and 532.60 eV, respectively. The signal at 529.14 eV indicates the lattice oxygen bonds, as (C=C)–C–O–Bi. The peaks at 529.79 eV and 530.38 eV correspond to the oxygen vacancies O–Mg and O–Fe in MFB, respectively. A peak at 532.60 eV is also observed, which is attributed to the carboxylate groups of the BTC bond or surface-adsorbed oxygen species. A peak at 532.70 eV is also observed, which is attributed to carboxylate groups of BTC linkers or surface-adsorbed oxygen species.[28,29] The Bi 4f spectrum (Fig. 4d) displays two peaks at 157.40 eV (Bi $4f_{7/2}$) and 162.70 eV (Bi $4f_{5/2}$), with a spin–orbit splitting of 5.3 eV, characteristic of Bi^{3+} species and confirming the formation of O–Bi–O bonds within the MOF framework.[26] The Fe 2p high-resolution spectrum (Fig. 4e) shows peaks at 709.30 eV and 722.90 eV, corresponding to Fe $2p_{3/2}$ and Fe $2p_{1/2}$, respectively. The ~13.6 eV separation between these two peaks is in good agreement with that of spinel-type ferrites, confirming the presence of Fe^{3+} in the $MgFe_2O_4$ lattice.[30] The Mg 2p spectrum

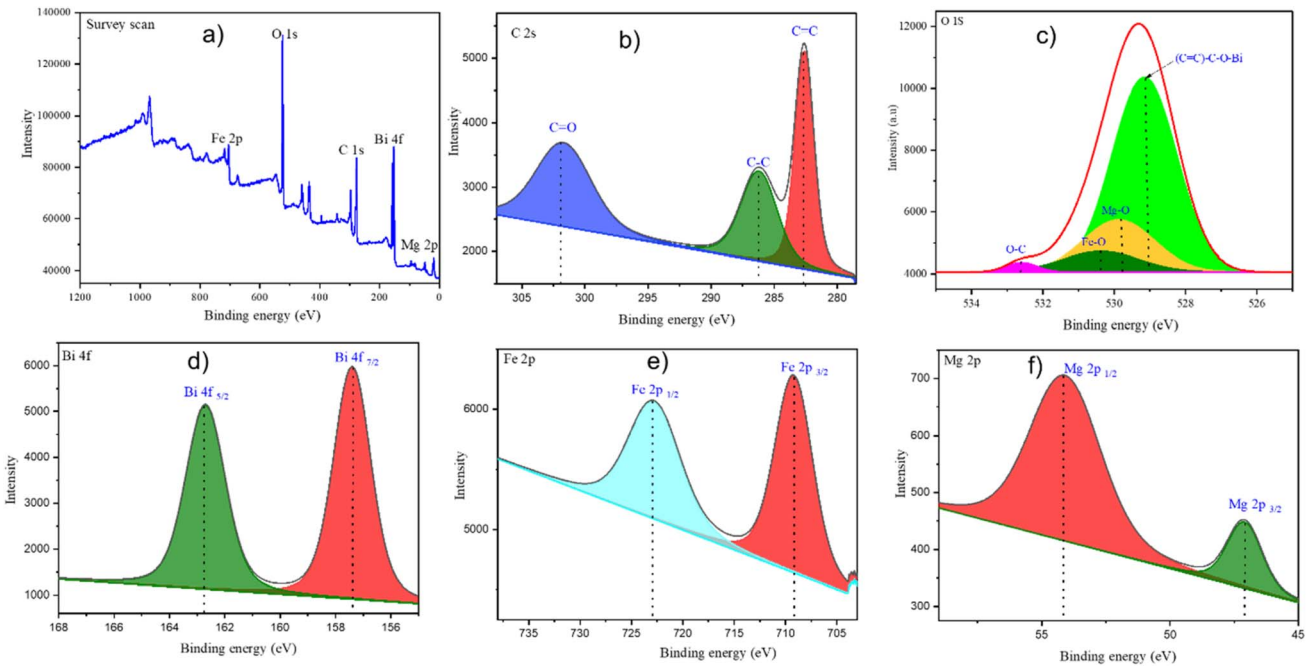

Fig. 4 XPS spectra of the MFB sample: (a) survey spectrum, (b) C 2s, (c) O 1s, (d) Bi 4f, (e) Fe 2p, and (f) Mg 2p.

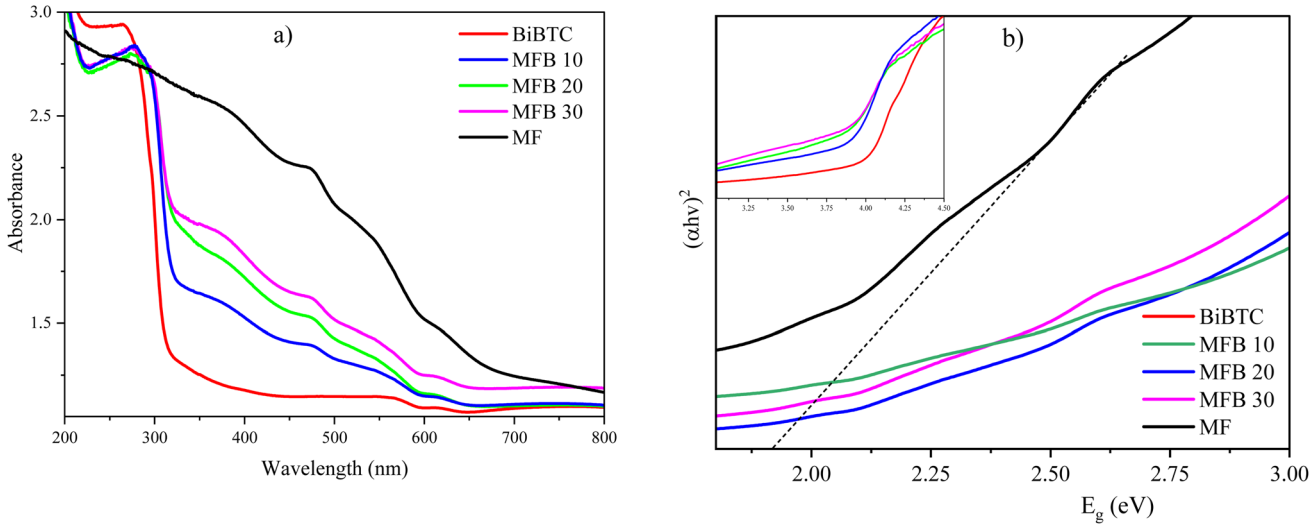

Fig. 5 Optical properties of the prepared samples: (a) UV-visible diffuse reflectance spectrum and (b) the corresponding Tauc plot for the indirect bandgap energy of the samples.

(Fig. 4f) reveals two binding energy peaks at 47.11 eV and 54.15 eV, which are assigned to Mg^{2+} ions occupying tetrahedral and octahedral sites, respectively, within the spinel structure of $MgFe_2O_4$.[29,31]

The optical absorption properties of the sample studied using UV-vis DRS are shown in Fig. 5a. The BiBTC material exhibits strong absorption in the range of 300–450 nm with a sharp edge around 400 nm, which is consistent with previous studies.[21,27] In contrast, $MgFe_2O_4$ displays broader absorption extending into the visible region at a wavelength of 500–670 nm, attributable to its narrower bandgap and spinel ferrite structure. The interaction between MF and BiBTC expanded the light absorption range of BiBTC. The absorption edge of MFB increasingly red-shifted to longer wavelengths relative to the absorption wavelength of BiBTC as the MF dosage increased in the MFB10, MFB20, and MFB30 samples. This alteration signified an enhancement in visible light absorption capacity, resulting in band gap modification that ameliorated the limitations of BiBTC in harnessing the sunlight of the MFB hybrid. Tauc plot analysis (Fig. 5b) reveals that the estimated indirect bandgap energies decrease in the following order: BiBTC > MFB10 > MFB20 > MFB30 > MF. Specifically, the bandgap of BiBTC is around 3.57 eV, while MF shows a significantly lower bandgap of ~1.93 eV. The MFB composites display reduced bandgap energies ranging from ~2.6 eV (MFB10) to ~2.2 eV (MFB30), confirming the synergistic interaction between the MOF matrix and the ferrite component.

The morphology was observed using SEM (Fig. 6). The SEM images of the MF material show a uniform distribution of spherical particles of $MgFe_2O_4$ ferrite nanoparticles, as shown in Fig. 6a and b. The structure appears dense and compact, with rough surfaces and grain sizes in the sub-100 nm range. This morphology provides high surface area and magnetic uniformity, which is favorable for further composite integration. The BiBTC material exhibits a well-defined rod-like crystal morphology, typical of MOF structures such as CAU-17 and UU-200. The rods are micrometer-scale in length and uniformly distributed, forming a highly porous, crystalline network. The smooth surfaces and ordered alignment indicate high crystallinity and phase purity of the BiBTC framework (Fig. 6c and d). SEM images of the MFB sample present the rod-like morphology of BiBTC and are partially coated and embedded with $MgFe_2O_4$ nanoparticles. These nanoparticles manifest as diminutive particle domains, either firmly adhering to or distributed throughout the BiBTC surface, facilitating charge transfer between MF and BiBTC, hence augmenting the visible light absorption capacity of MBF. The MF/BiBTC mass ratio influences the absorption capacity of MFB; excessive MF results in high coverage, restricting MFB's light absorption. The MFB20 sample meets the equilibrium criteria for light absorption, heterojunction area, and diffusion, indicating a strong photocatalytic capacity. The hybrid structure suggests successful physical integration of MF into the MOF matrix without significantly disrupting the BiBTC framework (Fig. 6e and f).

The elemental composition of the MFB composite was analyzed by SEM-EDS, as illustrated in Fig. 7a and b. The EDS spectrum reveals the presence of Mg (0.77%), Fe (2.78%), O (30.51%), C (45.51%), and Bi (20.44%), indicating the successful incorporation of $MgFe_2O_4$ into the BiBTC framework. These values are in good agreement with the surface composition determined from XPS analysis, confirming consistency between bulk and surface elemental distributions. Fig. 7c–i display the EDS elemental mapping of O, Bi, C, Fe, and Mg. The elemental maps demonstrate a homogeneous distribution of all elements throughout the composite matrix. Notably, the uniform dispersion of Mg and Fe suggests that the nanoscale magnesium ferrite phase is well-integrated within the BiBTC structure, ensuring efficient interaction between the MOF and ferrite domains. This uniformity is essential for achieving enhanced photocatalytic performance and magnetic recovery properties in the MFB composite.

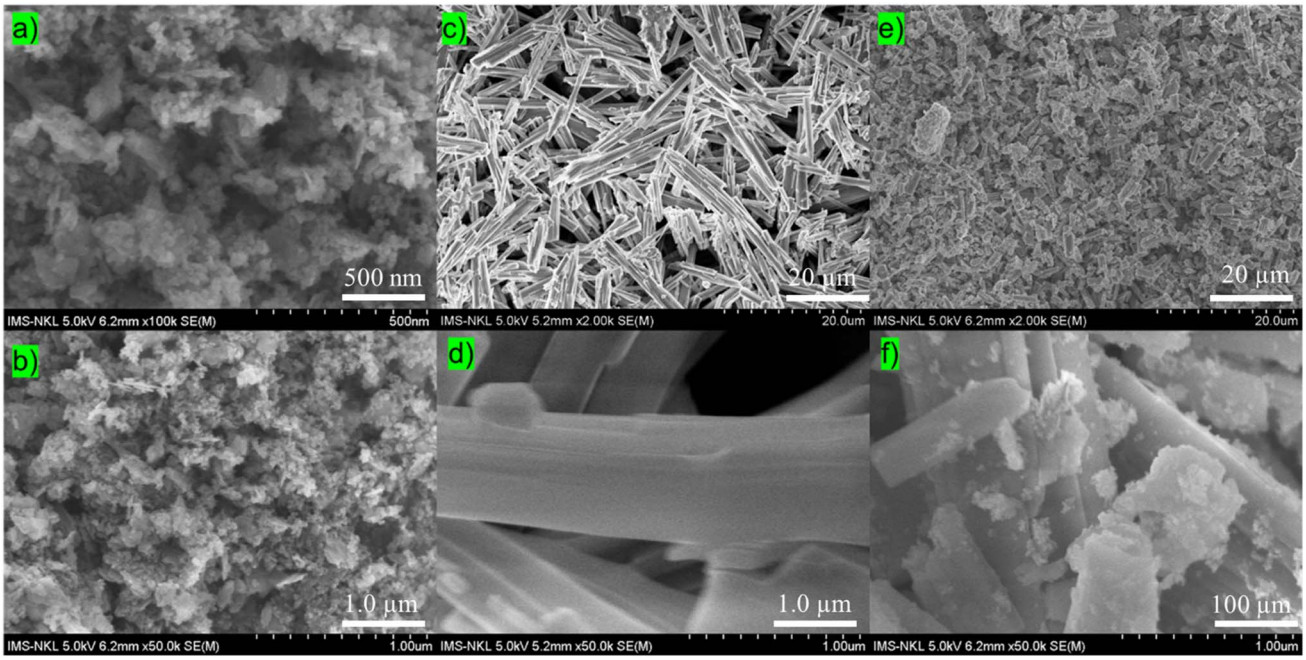

Fig. 6 SEM images of (a and b) MF, (c and d) BiBTC, (e and f) MFB.

Photocatalytic activity evaluation

The photocatalytic performance of MF, BiBTC, and the MFB composites (MFB10, MFB20, and MFB30) was investigated by degradation of rhodamine B under visible light irradiation. As illustrated in Fig. 8a and b, during the initial 60-minute dark adsorption phase, the materials reached near adsorption–desorption equilibrium within the first 30 min, removing approximately 10–20% of RhB. Only a slight increase in adsorption was observed in the subsequent 30 min. Upon 180 min of visible light exposure, BiBTC demonstrated substantial photocatalytic activity with a RhB degradation efficiency of 92.41%. Incorporation of $MgFe_2O_4$ into the BiBTC matrix further enhanced the photocatalytic performance. MFB10 and MFB20 achieved RhB degradation efficiencies of 94.23 and 97.98%, respectively, corresponding to MF/BiBTC mass ratios of 10 and 20%. Interestingly, MFB30, with 30% MF content, exhibited a decreased efficiency of 84.35%. These results suggest that the photocatalytic activity of the composites is sensitive to the MF loading. Moderate incorporation of MF enhances the catalytic activity by introducing additional active sites and improving charge carrier separation. The combined UV-vis DRS and XPS analyses support this enhancement, revealing that the MFB composites can absorb across both UV and visible regions and exhibit electronic interactions between MF and BiBTC. The formation of a heterojunction between the

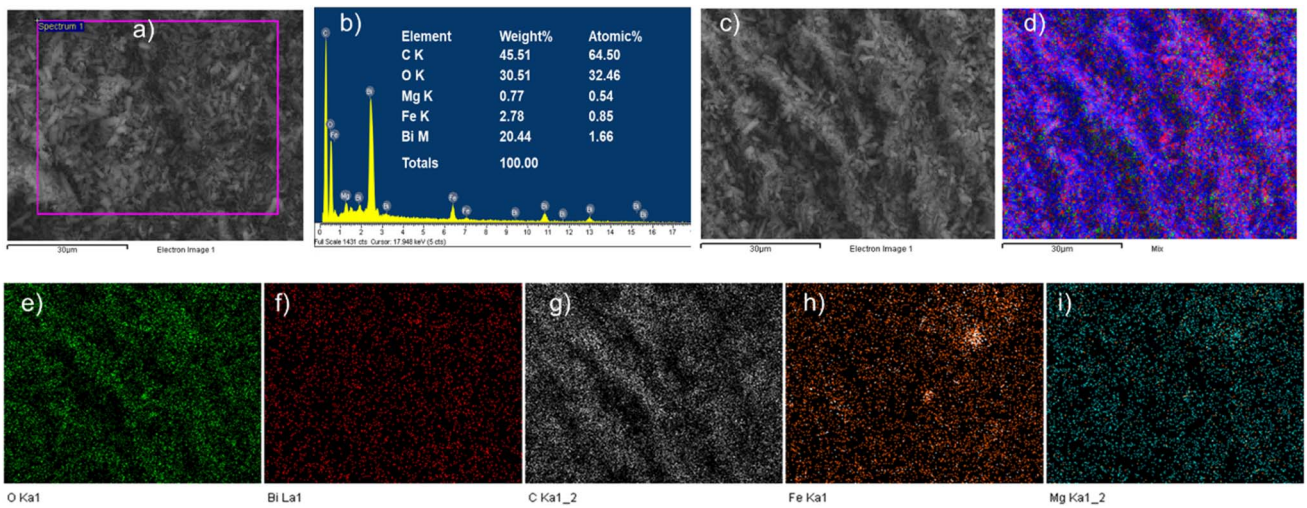

Fig. 7 (a and b) The EDX spectra and (c–i) elemental mapping of MFB.

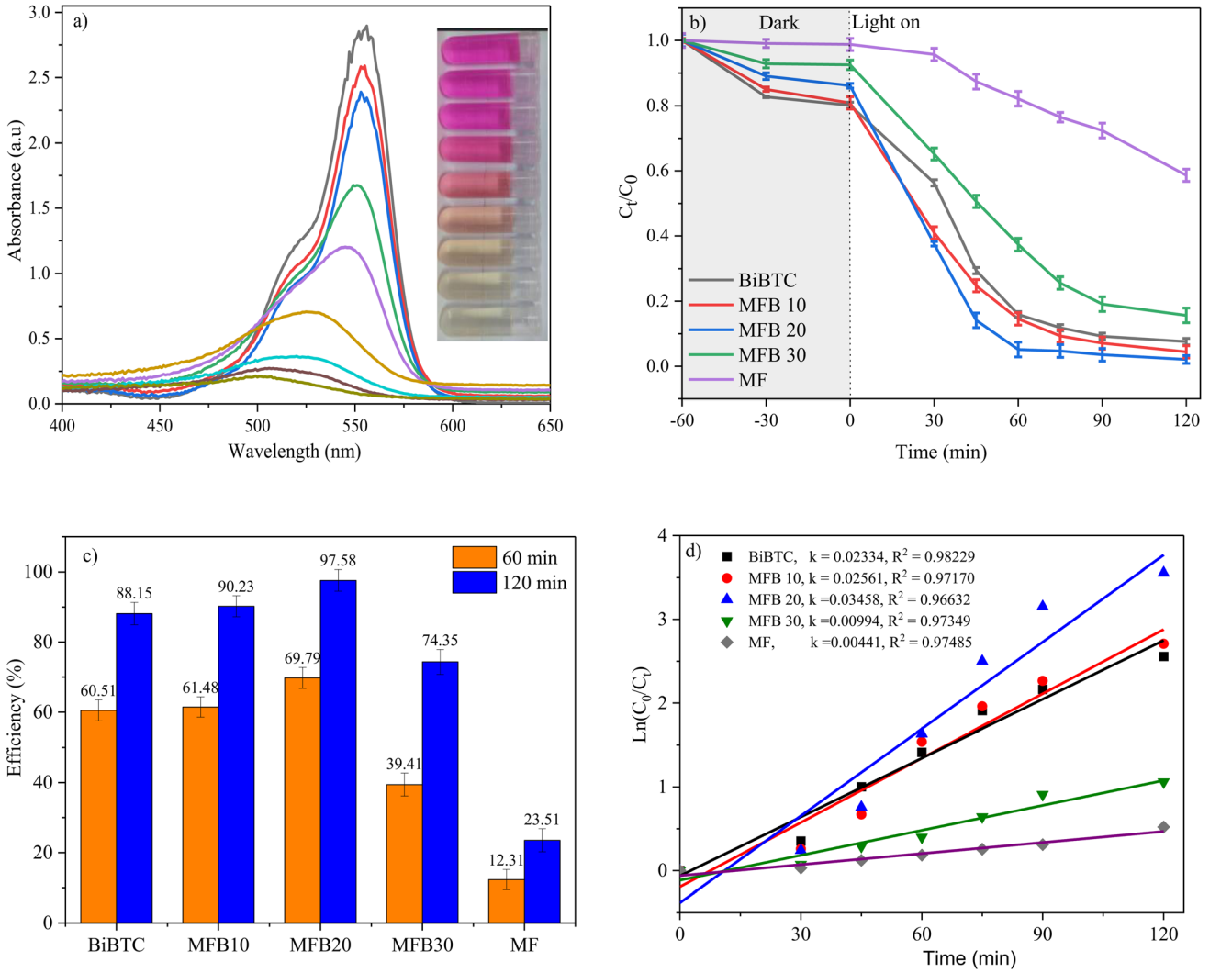

Fig. 8 (a) Absorbance drops under light irradiation, (b) C_t/C_0 *vs.* irradiation time plots, (c) effect of photodegradation-dependent discolorations, and (d) $\ln(C_0/C_t)$ *vs.* irradiation time curves using the as-synthesized samples. Conditions: [catalyst] = 10 mg, $V_{RhB\ 20\ mg\ L^{-1}}$ = 50 mL, light source: white LED (4 × 10 W).

two phases facilitates efficient charge transfer, generating intermediate energy levels that suppress the recombination of photogenerated electron–hole pairs. However, as in MFB30, excessive MF content can lead to a shielding effect at the MF–BiBTC interface, impeding light absorption and reducing photocatalytic performance. Therefore, MFB20, with its optimal balance of visible light absorption and interfacial interaction, was identified as the most efficient photocatalyst and selected for further application studies.[32,33] Fig. 8c presents the RhB degradation efficiencies of the synthesized materials following 120 min of visible light irradiation. Notably, within the first 60 min, all MFB composites exhibited rapid photocatalytic activity, with MFB20 achieving the highest degradation efficiency of 69.79%. However, the rate of RhB removal decreased over the subsequent 60 min, suggesting a reduction in available active sites or dye molecule concentration over time. Kinetic analysis of RhB photodegradation, shown in Fig. 8d, reveals that the degradation behavior for all samples closely follows a pseudo-first-order kinetic model, with correlation coefficients (r^2) ranging from 0.96632 to 0.98229. The calculated apparent rate constants (k) indicate the photocatalytic activity in the following order: MFB20 (k = 0.03458 min^{-1}) > MFB10 (k = 0.02561 min^{-1}) > BiBTC (k = 0.02334 min^{-1}) > MFB30 (k = 0.00994 min^{-1}) > MF (k = 0.00441 min^{-1}). These findings confirm that the synergistic interaction between $MgFe_2O_4$ and BiBTC in the MFB20 composite significantly enhances the degradation kinetics of RhB under visible light.

Effect of catalyst mass

Fig. 9a illustrates the influence of catalyst dosage on the photocatalytic degradation of RhB using MFB20. When the catalyst mass was increased from 5 to 20 mg, the degradation efficiency after 120 min of visible light irradiation improved from 76.71 to 97.98%. A significant enhancement was observed as the catalyst mass increased from 5 to 10 mg, achieving 97.58% degradation. However, further increases to 15 mg and 20 mg resulted in only

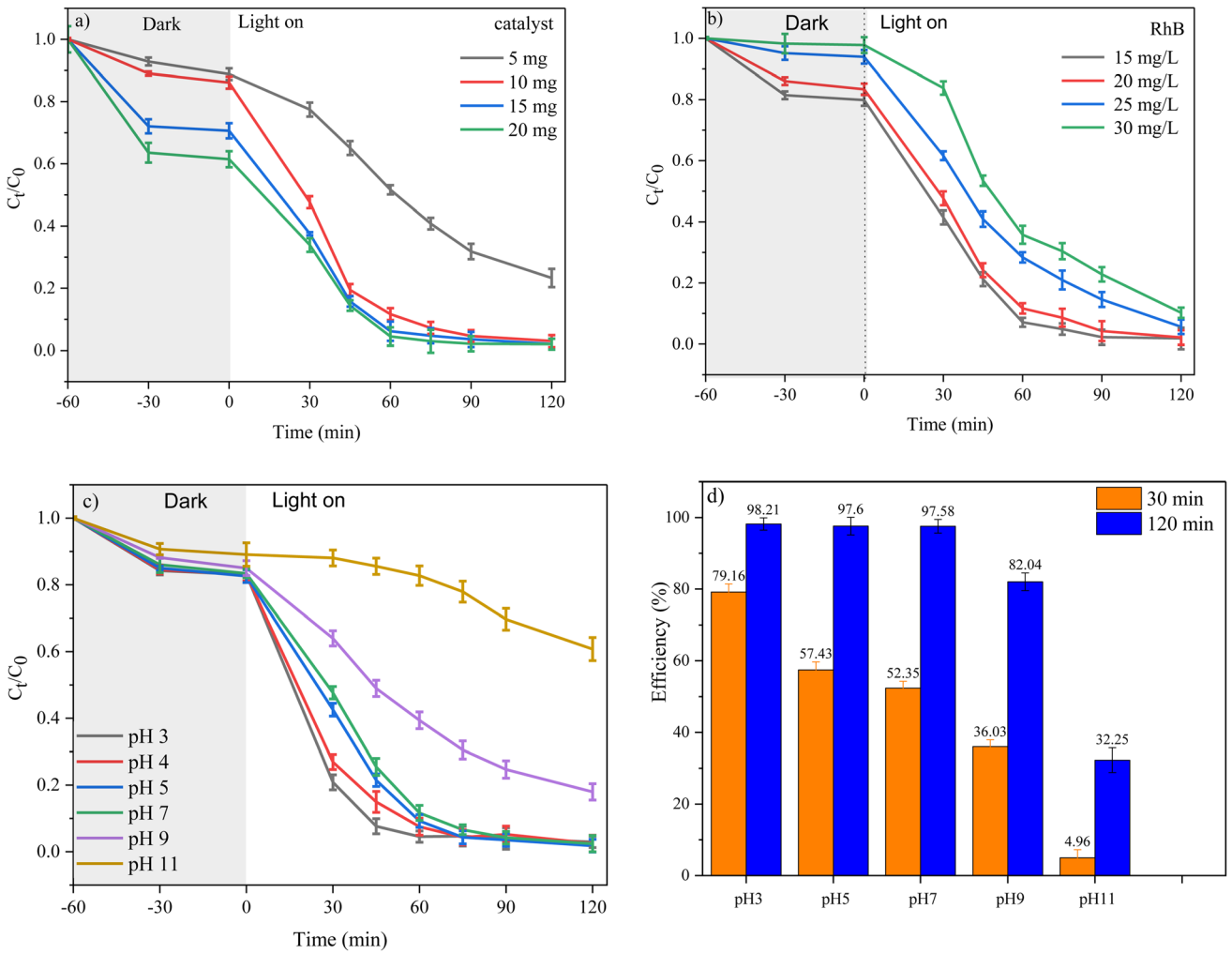

Fig. 9 (a) Effect of catalyst mass (conditions: catalyst: 5–20 mg, $V_{RhB\ 20\ mg\ L^{-1}} = 50$ mL). (b) Effect of initial concentration (conditions: initial concentration = 15–30 mg L^{-1}, $V_{RhB} = 50$ mL; catalyst mass: 10 mg) and (c and d) effect of pH (conditions: pH 3–11, $V_{RhB\ 20\ mg\ L^{-1}} = 50$ mL; catalyst mass: 10 mg).

marginal improvements, reaching 97.95 and 97.98%, respectively. The initial enhancement is attributed to the increased number of available active sites, which accelerates the adsorption and subsequent degradation of RhB. However, beyond 10 mg, the efficiency plateaued due to excessive catalyst loading. At higher concentrations, particle agglomeration and increased light scattering reduce the effective light penetration and photon absorption by the catalytic center.[34] Additionally, the higher turbidity of the suspension at elevated dosages may hinder mass transfer and reduce photocatalytic activity.[35] Based on this observation, 10 mg of MFB20 was selected as the optimal catalyst dosage for subsequent experiments.

Effect of initial dye concentration on photocatalytic degradation

The initial dye concentration plays a critical role in determining photocatalytic performance. In this study, RhB concentrations of 15, 20, 25, and 30 mg L^{-1} were evaluated while maintaining constant conditions: 10 mg of MFB20, 50 mL RhB solution, 60 min of dark adsorption, and 120 min of visible light irradiation. As shown in Fig. 9b, an increase in initial dye concentration led to a gradual decline in degradation efficiency. Specifically, the efficiencies at 15, 20, 25, and 30 mg L^{-1} were 98.17, 97.58, 94.37, and 89.78%, respectively. At lower concentrations (15–20 mg L^{-1}), nearly complete degradation was achieved, indicating efficient utilization of the available active sites and photon energy. However, as the dye concentration increased to 25 and 30 mg L^{-1}, the photocatalytic efficiency declined. This can be attributed to saturation of the active sites on the catalyst surface and limited photon flux. Since the number of photons and catalytic centers remains constant, excess dye molecules compete for active sites, reducing overall efficiency.[5,35] Additionally, high dye concentrations may lead to increased light absorption by the dye itself, limiting photon penetration to the catalyst surface and further inhibiting the generation of reactive species.

Effect of solution pH on photocatalytic activity

The influence of pH on the photocatalytic degradation of RhB by MFB20 was investigated at pH values of 3, 5, 7, 9, and 11. As shown in Fig. 9c and d, the degradation efficiencies after 30 min of visible light irradiation were 79.16, 57.43, 52.35, 36.03, and 4.96%, respectively, while the corresponding efficiencies after 120 min were 98.21, 97.60, 97.58, 82.04, and 32.25%. These results demonstrate that the MFB20 composite exhibits optimal photocatalytic performance under acidic conditions, with a marked decline in activity as the pH increases. This pH-dependent behavior is attributed to the ionization state of rhodamine B (RhB), an acidic dye that can exist in both zwitterionic ($RhB^{\pm}$) and cationic (RhB^{+}) forms depending on the solution pH. Under acidic conditions, RhB primarily exists in the cationic form (RhB^{+}), which is more readily adsorbed onto the negatively charged surface of MFB20 due to favorable electrostatic interactions.[32,36] Additionally, π–π stacking interactions between the aromatic rings of RhB and the conjugated structures within the MFB20 framework further enhance adsorption, improving photocatalytic degradation efficiency.[37,38] Conversely, in neutral to basic conditions, RhB predominantly exists in its zwitterionic form ($RhB^{\pm}$), wherein internal electrostatic interactions between carboxylate (−) and xanthene (+) groups reduce its ability to adsorb onto the catalyst surface. This weak interaction leads to a substantial decrease in photocatalytic efficiency under alkaline conditions.[34]

The performance of $MgFeO_4$, a well-researched visible-light photocatalyst, is frequently hindered by a low density of surface-active sites and rapid electron–hole recombination. In this study, we present the purposeful hybridization of $MgFeO_4$ with a Bi-based MOF (BiBTC), resulting in a bimetallic photocatalyst combining magnetic recyclability and vigorous photocatalytic activity. The resulting $MgFe_2O_4$@BiBTC performs favorably with the most advanced TiO_2, g-C_3N_4, and MOF-based systems, achieving near-complete RhB degradation under visible light with low catalyst dose (Table 1). This results from the robust synergy between $MgFe_2O_4$ and BiBTC, which improves visible-light absorption, promotes interfacial charge transfer, and accelerates pollutant adsorption, hence reducing recombination and increasing overall efficiency.

Stability and reusability

The long-term stability and reusability of the MFB20 composite were evaluated through four consecutive photocatalytic degradation cycles of RhB under visible light, as illustrated in Fig. 10. After each cycle, the catalyst was separated by magnetic recovery, thoroughly washed, dried, and reused under identical conditions. Fig. 10a shows the degradation kinetics across the four cycles. The MFB20 composite retained high photocatalytic efficiency, with only a slight reduction observed after the fourth cycle. As depicted in Fig. 10b, the degradation efficiencies for the first to fourth cycles were 97.98, 97.58, 92.42, and 90.61%, respectively. The results demonstrate that MFB20 maintains excellent photocatalytic activity and structural integrity over multiple uses, highlighting its durability and practical applicability. The RhB degradation efficiency of the MFB20 sample diminished by around 4.43% after four reuses, likely attributable to nanoparticle aggregation, which may modify the surface area, reducing active sites and decreasing the material's light absorption capability. A further potential cause is that accumulating intermediates or organic by-products on the catalyst surface during reuse may obscure the photocatalytic active sites. The presence of magnetic $MgFe_2O_4$ facilitates easy recovery using an external magnet, minimizing material loss and making the system advantageous for repeated environmental remediation applications. The XRD patterns (Fig. 10c) indicate that the characteristic diffraction peaks of MFB20 are retained after both the first and fourth cycles. The major reflections corresponding to the spinel $MgFe_2O_4$ phase and BiBTC framework remain clearly observable without noticeable peak broadening or shifting, suggesting that the crystalline structure of the composite remains intact. Similarly, the FT-IR spectra (Fig. 10d) of MFB20 after photocatalytic cycles show all key vibrational bands associated with the functional groups of BiBTC and $MgFe_2O_4$. The bands corresponding to Bi–O stretching, carboxylate groups of the BTC linker, and metal–oxygen (Fe–O and Mg–O) vibrations are preserved across all samples, with only minimal changes in intensity. This further confirms the retention of chemical bonding environments and the integrity of the hybrid framework during recycling.

Table 1 Comparison of the photocatalytic efficiency of RhB dye degradation using various materials

Catalyst	Catalyst amount	RhB concentration	Time (min)	Light source	Degradation efficiency (%)	Ref.
TiO_2	100 mg	10 mg L^{-1}	45	Xenon lamp (250 W)	99.6	39
ZnO–TiO_2	100 mg	20 mg L^{-1}	60	Xenon lamp (350 W)	85	40
Ag_3PO_4/N-TiO_2	20 mg	10 mg L^{-1}	120	Xenon lamp (50 W)	91	41
3D TiO_2@PDMS	385–400 mg	10^{-5} M	600	SF300-A small collimated beam	100	42
g-C_3N_4/UU-200	10 mg	3×10^{-5} M	90	Cree Xlamp XM-L2 LEDs (40 W)	97.5	43
TiO_2/BiBTC-MOFs	0.4 g L^{-1}	5 mg L^{-1}	40	Visible light	98.86	44
GO@BiBTC MOF	10 mg	15 mg L^{-1}	60	LED light	98	45
Ag/AgCl-NW/rGO	30 mg	10 mg L^{-1}	120	Halogen lamp (300 W)	99.78	46
$MgFe_2O_4$@BiBTC	10 mg	20 mg L^{-1}	120	LED light (40 W)	97.98	This work

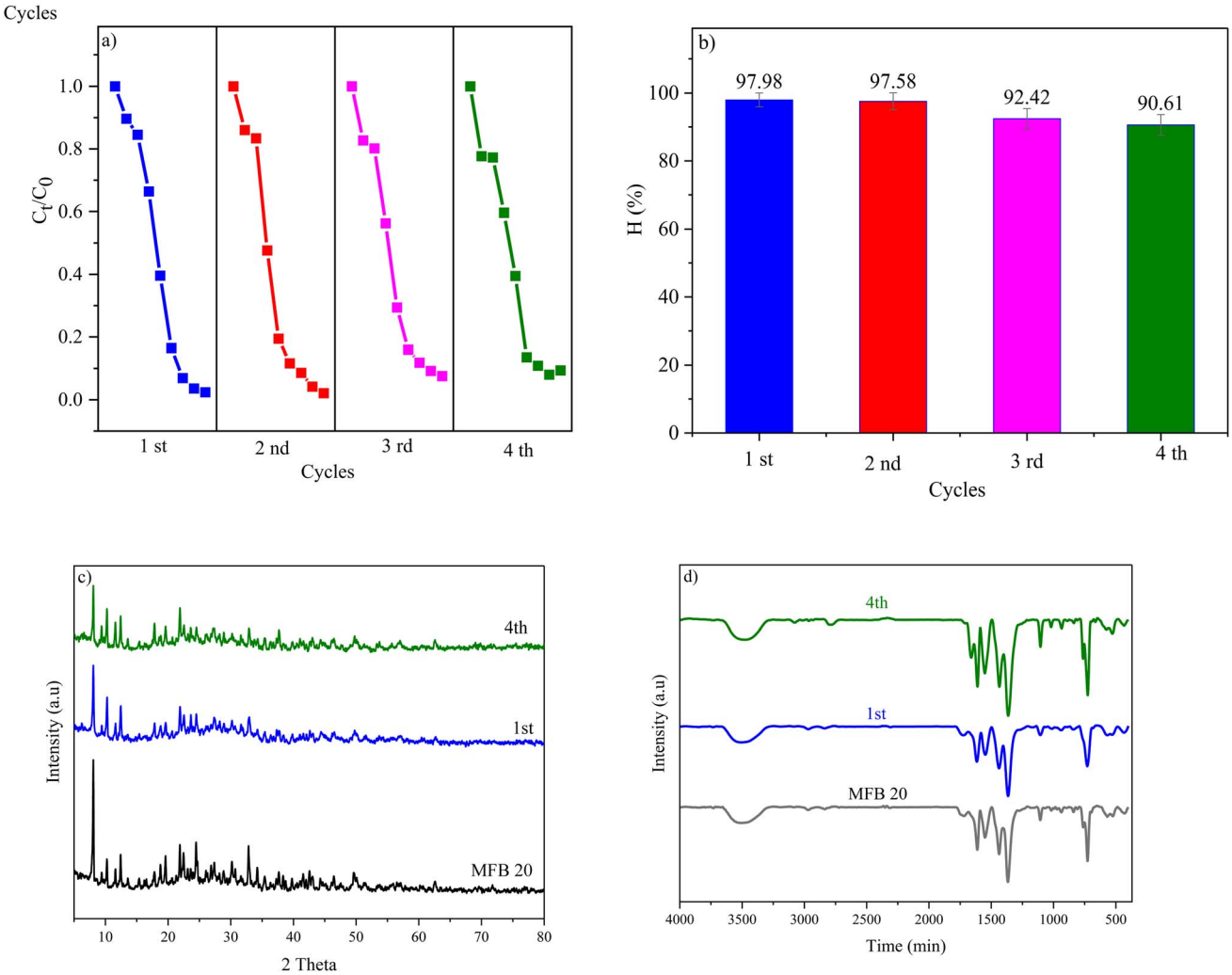

Fig. 10 (a and b) RhB photodegradation efficiency (conditions: catalyst 10 mg, $V_{\text{RhB 20 mg L}^{-1}} = 50$ mL); (c) XRD pattern, and (d) FT-IR of the used catalyst.

Reactive species trapping and photocatalytic mechanism

The roles of various reactive species involved in the photocatalytic degradation of RhB by MFB20 were investigated using scavenger experiments, as illustrated in Fig. 11. The addition of specific scavengers: ethanol for hydroxyl radicals ($^{\bullet}$OH), sodium oxalate for photogenerated holes (h^+), and potassium dichromate for electrons (e^-) led to a moderate decrease in degradation efficiency, resulting in RhB removal rates of 90, 84, and 73%, respectively. However, upon introducing 100 μM of benzoquinone, a known scavenger for superoxide radicals ($O_2^{\bullet-}$), the degradation efficiency markedly declined to approximately 46%. This significant reduction highlights the dominant role of superoxide radicals in the photocatalytic process. These results suggest that the primary oxidative species responsible for RhB degradation is $O_2^{\bullet-}$, while e^-, h^+, and $^{\bullet}$OH contribute to a lesser extent. The order of radical contribution to the degradation process can thus be summarized as follows: $O_2^{\bullet-} > e^- > h^+ > {}^{\bullet}OH$. This mechanistic insight confirms that the enhanced activity of MFB20 is closely associated with efficient generation and utilization of superoxide radicals under visible light irradiation.

According to the findings in Fig. 5b, MF and BiBTC have E_g of 1.93 eV and 3.57 eV, respectively. The reduction potentials of MF at the valence band (VB) and conduction band (CB) are calculated using eqn (1) and (2), yielding values of $E_{VB} = 0.545$ eV and $E_{CB} = -1.385$ eV.

$$E_{VB} = \chi - E_e + 0.5E_g \quad (1)$$

$$E_{CB} = E_{VB} - E_g \quad (2)$$

In which χ represents the electronegativity of MF, determined at 4.08 eV,[47] whereas E_c denotes the free electron energy on the hydrogen electrode scale (4.5 eV). The VB and CB reduction potentials are $E_{VB} = 3.0$ eV and $E_{CB} = -0.43$ eV, respectively, as per our previous studies.[48] Based on the reactive species trapping data and light absorption characteristics, photocatalytic pathways are described in Fig. 12. UV-vis study verified that the MFB20 composite demonstrates light

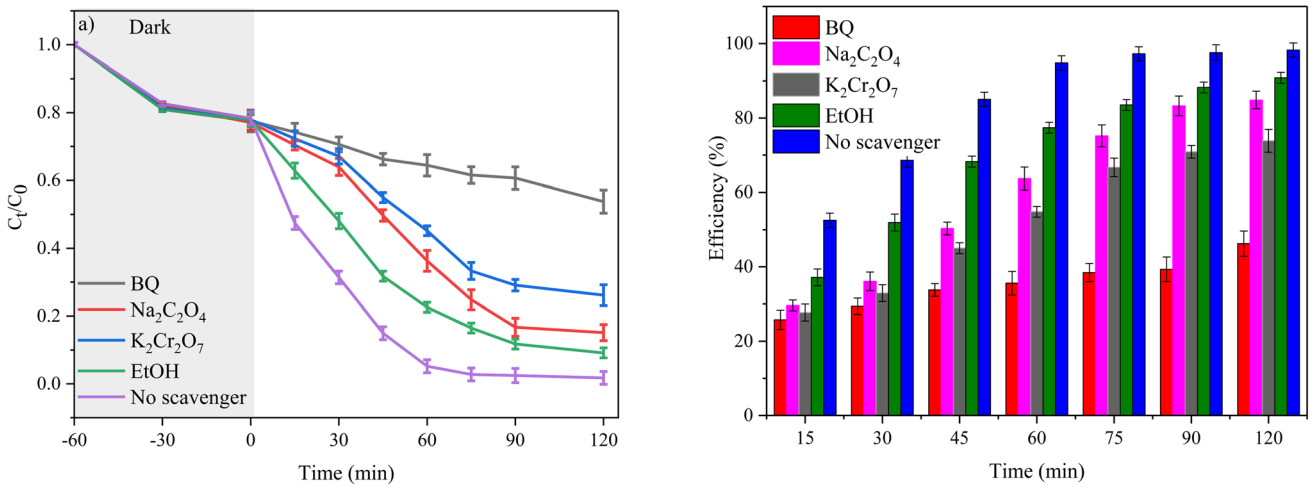

Fig. 11 The photocatalytic RhB degradation without and with radical scavengers (a) C_t *vs.* C_0 and (b) photodegradation efficiency.

absorption in the ultraviolet and visible spectra, forming photogenerated electron–hole pairs. At the heterojunction of the two phases, the reduction potential of MF at CB ($E_{CB} = -1.385$ eV) is more negative than that of BiBTC ($E_{CB} = -0.43$ eV), resulting in the transfer of electrons from the CB of MF to the CB of BiBTC, together with BiBTC's electrons, capture O_2 to generate $O_2^{\bullet-}$ ($E_{O_2/O_2^-} = -0.33$ eV), causing the decomposition of RhB. Furthermore, the electrons in the CB of MF may also combine with O_2 to generate $O_2^{\bullet-}$, leading to the decomposition of RhB. In the VB, the reduction potential of BiBTC ($E_{VB} = 3.0$ eV) is more positive than the reduction potential of MF ($E_{VB} = 0.545$ eV); therefore, the photogenerated BiBTC holes migrate to MF. Nevertheless, these holes directly break down RhB. The experimental evidence indicates that $O_2^{\bullet-}$ is the primary agent in the photocatalytic degradation of RhB by MFB20. The amalgamation of MF and BiBTC facilitated efficient charge separation, enabling the movement of electrons and holes over the interface, hence inhibiting recombination and extending the lifespan of the charge carriers. The degradation mechanism can be described through the following photochemical reactions:

$$\text{MFB20} + h\nu \rightarrow \text{MFB20}(e^-, h^+)$$

$$\text{MFB20}(e^-) + \text{RhB} \rightarrow \text{product}$$

$$\text{MFB20}(e^-) + O_2 \rightarrow O_2^{\bullet-}$$

$$O_2^{\bullet-} + \text{RhB} \rightarrow \text{product (main reaction)}$$

$$\text{MFB20}(h^+) + \text{RhB} \rightarrow \text{product}$$

$$\text{MFB20}(h^+) + 2H_2O \rightarrow OH^{\bullet} + H^+$$

$$OH^{\bullet} + \text{RhB} \rightarrow \text{product}$$

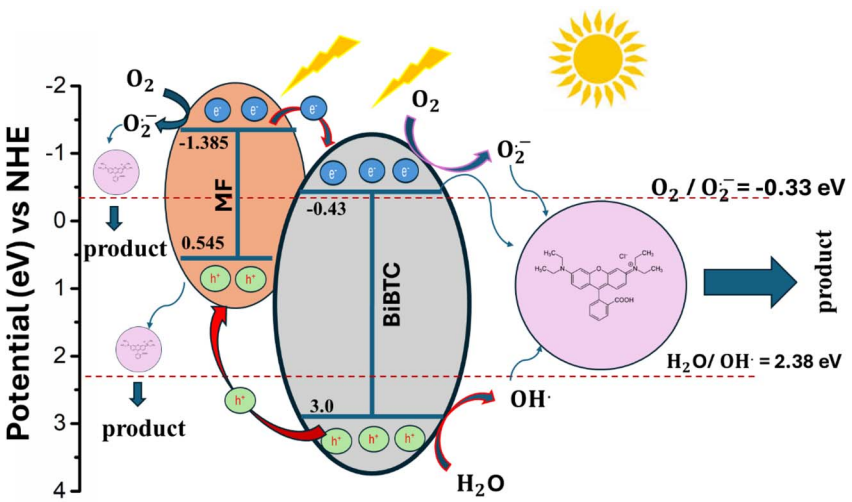

Fig. 12 The proposed photocatalytic mechanism over the synthesized MFB catalyst.

Conclusions

In this study, a novel $MgFe_2O_4$/BiBTC composite was successfully synthesized *via* a straightforward room-temperature method and evaluated as an efficient photocatalyst for the degradation of rhodamine B under visible light irradiation. Structural and morphological analyses using XRD, FT-IR, SEM-EDS, and XPS confirmed the successful integration of $MgFe_2O_4$ into the BiBTC framework without compromising crystallinity or chemical integrity. Among the composites tested, MFB20 exhibited the highest photocatalytic performance, achieving a 97.98% degradation efficiency after 120 min, attributed to its optimal heterojunction interface and enhanced charge separation. The photocatalytic activity of MFB20 was strongly influenced by catalyst dosage, initial dye concentration, and solution pH, with acidic conditions and moderate catalyst loading providing the best performance. Radical scavenging experiments identified superoxide radicals ($O_2^{\bullet-}$) as the dominant reactive species in the degradation process. Furthermore, MFB20 demonstrated excellent reusability and structural stability over multiple cycles, as evidenced by consistent catalytic activity and retained structural features in post-catalysis XRD and FT-IR analyses. This work highlights the potential of MFB20 as a promising, reusable, and visible-light-responsive photocatalyst for organic pollutant degradation in wastewater treatment applications.

Author contributions

Van Cuong Nguyen: writing – review and editing; investigation; Trinh Duy Nguyen: conceptualization; validation; Nguyen Thi Mai Tho: writing – original draft, formal analysis; Ai Le Hoang Pham: investigation, methodology; Thi Huyen Thoa Pham: formal analysis and Huynh Dao Thanh Dreaml: methodology, formal analysis.

Conflicts of interest

The authors state that they have no interests that could have influenced the work reported in this study.

Data availability

All data and materials generated or analyzed during this study are included in this published article.

Acknowledgements

This research is supported by Industrial University of Ho Chi Minh City (IUH) under grant number 105/HĐ-ĐHCN, and we acknowledge Nguyen Tat Thanh University, Ho Chi Minh City, Vietnam, for facilities support.

References

1 L. M. Skjolding, L. v. G. Jørgensen, K. S. Dyhr, C. J. Köppl, U. S. McKnight, P. Bauer-Gottwein, P. Mayer, P. L. Bjerg and A. Baun, *Water Res.*, 2021, **197**, 117109.
2 P. O. Oladoye, M. Kadhom, I. Khan, K. H. Hama Aziz and Y. A. Alli, *Green Chem. Eng.*, 2024, **5**, 440–460.
3 B. Lellis, C. Z. Fávaro-Polonio, J. A. Pamphile and J. C. Polonio, *Biotechnol. Res. Innovation*, 2019, **3**, 275–290.
4 Md. M. Islam, A. R. Aidid, J. N. Mohshin, H. Mondal, S. Ganguli and A. K. Chakraborty, *Cleaner Chem. Eng.*, 2025, **11**, 100165.
5 A. Chakraborty, B. Bhattacharjee and Md. Ahmaruzzaman, *Inorg. Chem. Commun.*, 2025, **171**, 113444.
6 H. A. Le Pham, T. K. Vo, D. T. Nguyen, H. K. Huynh, Q. T. S. Pham and V. C. Nguyen, *Green Chem. Lett. Rev.*, 2022, **15**, 572–581.
7 A. V Mohod, M. Momotko, N. Samad and M. Marchel, *Water Resour. Ind.*, 2023, **30**, 100220.
8 P. Yi, Y. Li, X. L. Wu and X. Duan, *Curr. Opin. Chem. Eng.*, 2024, **45**, 101028.
9 I. Sebah and M. Belmouden, *Nanoscale Adv.*, 2025, **7**, 5646–5657.
10 J. Liu, H. Wang, M.-J. Chang, M. Sun, Z.-W. He, C.-M. Zhang, W.-Y. Zhu, J.-L. Chen, H.-L. Du, L.-G. Peng, Z.-M. Luo and L. Zhang, *Colloids Surf., A*, 2022, **648**, 129299.
11 T. Zhou, X. Su, Y. Ou, R. Min, G. Zhang and M. Zhang, *Mater. Today Commun.*, 2025, **44**, 111969.
12 P. Garcia-Muñoz, F. Fresno, V. A. de la Peña O'Shea and N. Keller, *Top. Curr. Chem.*, 2020, **378**, 1–56.
13 Z. Jiang, K. Chen, Y. Zhang, Y. Wang, F. Wang, G. Zhang and D. D. Dionysiou, *Sep. Purif. Technol.*, 2020, **236**, 116272.
14 H. Tian, J. Peng, T. Lv, C. Sun and H. He, *J. Solid State Chem.*, 2018, **257**, 40–48.
15 L. Zhang, Y. He, Y. Wu and T. Wu, *Mater. Sci. Eng., B*, 2011, **176**, 1497–1504.
16 N. Huo, Y. Yin, W. Liu, J. Zhang, Y. Ding, Q. Wang, Z. Shi and S. Yang, *New J. Chem.*, 2016, **40**, 7068–7074.
17 X. Yuan, H. Wang, Y. Wu, X. Chen, G. Zeng, L. Leng and C. Zhang, *Catal. Commun.*, 2015, **61**, 62–66.
18 M. Köppen, A. Dhakshinamoorthy, A. K. Inge, O. Cheung, J. Ångström, P. Mayer and N. Stock, *Eur. J. Inorg. Chem.*, 2018, 3496–3503.
19 M. Åhlén, E. Kapaca, D. Hedbom, T. Willhammar, M. Strømme and O. Cheung, *Microporous Mesoporous Mater.*, 2022, **329**, 111548.
20 Z. Wang, Z. Zeng, H. Wang, G. Zeng, P. Xu, R. Xiao, D. Huang, S. Chen, Y. He, C. Zhou, M. Cheng and H. Qin, *Coord. Chem. Rev.*, 2021, **439**, 213902.
21 S. Dong, L. Wang, W. Lou, Y. Shi, Z. Cao, Y. Zhang and J. Sun, *Ultrason. Sonochem.*, 2022, **91**, 106223.
22 T. D. Nguyen, V. H. Nguyen, A. Le Hoang Pham, T. Van Nguyen and T. Lee, *RSC Adv.*, 2022, **12**, 25377–25387.
23 H. A. Le Pham, D. T. Nguyen, V. C. Nguyen and T. Ky Vo, *Inorg. Chem. Commun.*, 2024, **159**, 111822.
24 A. Loganathan and K. Kumar, *Appl. Sci.*, 2016, **6**, 629–639.

25 S. K. Durrani, S. Naz, M. Mehmood, M. Nadeem and M. Siddique, *J. Saudi Chem. Soc.*, 2017, **21**, 899–910.
26 R. Huang, Z. Zhou, X. Lan, F. K. Tang, T. Cheng, H. Sun, K. Cham-Fai Leung, X. Li and L. Jin, *Mater. Today Bio*, 2023, **18**, 100507.
27 Y. Li, Y. Han, H. Li, X. Niu, X. Liu, D. Zhang, H. Fan and K. Wang, *J. Colloid Interface Sci.*, 2024, **653**, 764–776.
28 R. Huang, Z. Zhou, X. Lan, F. K. Tang, T. Cheng, H. Sun, K. Cham-Fai Leung, X. Li and L. Jin, *Mater. Today Bio*, 2023, **18**, 100507.
29 B. Rahmanivahid, M. Pinilla-de Dios, M. Haghighi and R. Luque, *Molecules*, 2019, **24**, 2597.
30 N. Huo, Y. Yin, W. Liu, J. Zhang, Y. Ding, Q. Wang, Z. Shi and S. Yang, *New J. Chem.*, 2016, **40**, 7068–7074.
31 R. Revathi, M. Sukumar, A. Kumar, M. Gupta, P. A. Udhaya, S. S. Sehgal, B. Pandit, M. Sundararajan, A. Subramani, C. S. Dash, N. Senthilkumar and M. Ubaidullah, *J. Inorg. Organomet. Polym. Mater.*, 2024, **34**, 374–386.
32 J. Goswami, P. Basyach, S. K. Purkayastha, A. K. Guha, P. Hazarika and L. Saikia, *New J. Chem.*, 2023, **47**, 22304–22319.
33 F. Li, X. Dai, L. Zhang, Z. Zhang, H. Wu, J. Li and J. Guo, *J. Mater. Sci.: Mater. Electron.*, 2024, **35**, 463.
34 N. T. M. Tho, B. T. Huy, D. N. N. Khanh, H. N. N. Ha, V. Q. Huy, N. T. T. Vy, D. M. Huy, D. P. Dat and N. T. K. Phuong, *Korean J. Chem. Eng.*, 2018, **35**, 2442–2451.
35 Y. Ji, C. Zou, Y. Wang, Z. Zhou, M. Liu, Y. Xu, R. Liu and M. Yang, *J. Inorg. Organomet. Polym. Mater.*, 2024, **34**, 5791–5804.
36 Y. Guo, C. Zhou, L. Fang, Z. Liu, W. Li and M. Yang, *ACS Omega*, 2021, **6**, 8119–8130.
37 V. A. Tran, T. T. Sang, N. A. Thu, V. Vo, V. T. Le, V. D. Doan, T. T. Thi Vo and N. D. Dat, *RSC Adv.*, 2024, **14**, 31171–31182.
38 M. Shoaib, M. A. Munir, M. Y. Naz, G. Abbas, M. Irfan, S. Rahman and A. A. J. Ghanim, *Water, Air, Soil Pollut.*, 2023, **234**, 422.
39 M. Tang, Y. Xia, D. Yang, J. Liu, X. Zhu and R. Tang, *Materials*, 2021, **14**, 5674.
40 Y. Sun, Y. Gao, B. Zhao, S. Xu, C. Luo and Q. Zhao, *Mater. Res. Express*, 2020, **7**, 085010.
41 N. R. Khalid, U. Mazia, M. B. Tahir, N. A. Niaz and M. A. Javid, *J. Mol. Liq.*, 2020, **313**, 113522.
42 M. Enculescu, M. Beregoi, M.-C. Bunea, M.-M. Trandafir and I. Enculescu, *Results Eng.*, 2025, **27**, 107083.
43 T. D. Nguyen, V. H. Nguyen, A. Le Hoang Pham, T. Van Nguyen and T. Lee, *RSC Adv.*, 2022, **12**, 25377–25387.
44 S. Dong, L. Wang, W. Lou, Y. Shi, L. Li, Z. Cao, Y. Zhang and J. Sun, *J. Dispersion Sci. Technol.*, 2023, **44**, 2058–2069.
45 V. C. Nguyen, T. D. Nguyen, Q. Thanh Hoai Ta and A. L. H. Pham, *RSC Adv.*, 2025, **15**, 2779–2791.
46 C. Yarangsee, S. Narakaew, S. Utara, S. Thungprasert, T. Promanan and A. Chaisena, *Environ. Sci. Pollut. Res.*, 2025, **32**, 6658–6677.
47 K. M. Katubi, A. Murtaza, H. M. Asif, Z. A. Alrowaili, M. S. Al-Buriahi, S. Munir and M. F. Warsi, *J. Alloys Compd.*, 2024, **978**, 173327.
48 H. A. Le Pham, D. T. Nguyen, V. C. Nguyen and T. Ky Vo, *Inorg. Chem. Commun.*, 2024, **159**, 111822.